Research Article

Behavior of the T-Shaped Concrete-Filled Steel Tubular Columns after Elevated Temperature

Xianglong Liu,[1] Jicheng Zhang [ID],[1] Hailin Lu,[2] Ning Guan,[3] Jiahao Xiao,[1] and Guofeng Du[1]

[1]*School of Urban Construction, Yangtze University, Jingzhou 434023, China*
[2]*School of Civil Engineering and Architecture, Wuhan Institute of Technology, Wuhan 430000, China*
[3]*School of Mechanical and Storage Engineering, China University of Petroleum, Beijing 100000, China*

Correspondence should be addressed to Jicheng Zhang; zhangjicheng@yangtzeu.edu.cn

The mechanical properties of T-shaped concrete-filled steel tubular (TCFST) short columns under axial compression after elevated temperature are investigated in this paper. A total of 30 TCFST short columns with different temperature (T), steel ratio (α), and duration of heating (t) were tested. The TCFST column was directly fabricated by welding two rectangular steel tubes together. The study mainly investigated the failure modes, the ultimate bearing capacity, the load-displacement, and the load-strain performance of the TCFST short columns. Experimental results indicate that the rectangular steel tubes of the TCFST column have deformation consistency, and the failure mode consists of local crack, drum damage, and shear failure. Additionally, the influence of high temperature on the residual bearing capacity of the TCFST is significant, e.g., a higher temperature can downgrade the ultimate bearing capacity. Finally, a finite element model (FEM) is developed to simulate the performance of the TCFST short columns under elevated temperature, and the results agree with experimental values well. Overall, this investigation can provide some guidance for future studies on damage assessment and reinforcement of the TCFST columns.

1. Introduction

As one of the main components of buildings, concrete-filled steel tube (CFST) column has several advantages such as high rigidity, high strength, large capacity of energy absorption, and high ductility [1–3]. However, multiple damage forms (i.e., crack, debonding, drumming, and large deformation) [4–7] caused by various factors including the fire [8], aging [9], earthquake [4, 5], impact [6, 7], and corrosion [10–12], will downgrade the performance of CFST structures. Particularly, it is well known that physical properties such as the strength and stiffness of concrete and steel are greatly reduced when the CFST short column is subjected to elevated temperature. Thus, some researchers have conducted many experimental investigations on the mechanical properties (particularly the fire-resist performance and the residual bearing capacity) of CFST under elevated temperature [13, 14] and low temperature [15, 16]. For instance,

combining experiments and theoretical analyses, Han [1] proposed a practical calculation method for the bearing capacity of the CFST columns under elevated temperature. Yong et al. [17] researched the performance of the CFST column under the fire effect, and results revealed that thicker coating could enhance fire-resistance while a larger axial compression ratio made the opposite effect. Mahsa et al. [18] investigated the effect of elevated temperature on the mechanical properties of the ordinary concrete and steel-concrete composite structures, and they demonstrated that predeformation failed at high temperature. Other investigations [19–23] have also been reported to characterize the influence of elevated temperature on mechanical properties of the CFST. On the other hand, numerical analyses [24–27] were proposed to study the mechanical properties of the CFST under the effect of conflagration. According to the ISO 834 standard fire condition, Tan et al. [28] researched the mechanical behavior of the CFST column via finite element analysis

(FEA). Song and Han [29] developed a post-fire finite element (FE) model of the CFST column and steel beam joints, and they studied the mechanical properties of the CFST column during the whole heating process. Tao et al. [30] conducted an FE model of the CFST column to determine mechanical properties under the cases of in-fire and post-fire, and simulation results showed good agreement with experimental values.

In recent years, in order to meet the increasing requirements of the construction industry, a new type of composite column emerged at the historic moment which named special-shaped CFST column. The special-shaped CFST column inherits the advantages of traditional CFST and can be adapted to specific requirements of the building (e.g., avoiding the corners of the structure to make it more aesthetic). Moreover, the special-shaped CFST column can reduce the consumption of concrete and steel, thus achieving a better economic effect. Therefore, the special-shaped CFST has attracted wide attention in the field of civil engineering [31–33]. However, most current investigations of the mechanical properties of special-shaped CFST are limited to room temperature, rather than elevated temperatures. For instance, Ren et al. [34] analyzed the performance of a special-shaped CFST short column under axial load. Liu et al. [35] conducted axial compression experiments on the L-shaped and T-shaped CFST short columns, and experimental results revealed that the reinforced ribs could effectively prevent the local buckling of the steel tube and increase the buckling ability. Yang et al. [36] studied the effects of different internal cavities on the performance of multicavity giant CFST columns. Wang et al. [37] carried out an experimental study to investigate the hysteretic characteristics of the TCFST columns, including the failure mode, the hysteresis performance, and the reinforcement mechanism. Du et al. [38] applied cyclic loading to the TCFST column joints, and they found that the performance, ductility, and energy consumption of the hysteresis joint could be significantly improved by increasing the width of the reinforcing ring. Zhang and Yang [39] studied the influence of L-shaped CFST space frame under seismic loading.

So far, a large number of researchers have studied the mechanical properties of ordinary CFST column at different temperatures, or the experimental study of special-shaped CFST column at ambient temperature, but few studies focus on the property of the special-shaped CFST short column at elevated temperature. However, the steel bars inside the special-shaped columns are also affected by high temperatures. Therefore, fire safety should consider not only the normal CFST short column but also the special-shaped CFST short column. In this paper, we focus on studying the performance of the TCFST short column under axial compression after elevated temperature. The TCFST short columns are fabricated by welding two rectangular steel tubes. Thirty specimens were tested with different steel ratios, different temperatures, and different durations of heating. After suffering elevated temperature, specimens were subjected to axial compression. The failure mode, load-displacement relationship, load-strain relationship, and the ultimate bearing capacity of specimens

are analyzed. In addition, the calculation formula of bearing capacity is obtained by software fitting, and there was a great agreement with the experimental results. Finally, the experiment results are compared with numerical results obtained by finite element software. The investigations in this paper provide great guidance for fast repairing of building structures and reducing the economic loss after fire.

2. Experimental Program

2.1. Specimens Design.
A total of 30 TCFST short columns were designed and experimented. The TCFST column was directly fabricated by welding two rectangular steel tubes together. The steel ratio, the temperature, and the duration of heating were the main parameters in this study. The steel ratio is controlled by thickness of the steel tube, as shown in the following equation:

$$\alpha = \frac{A_s f_y}{A_c f_c}, \tag{1}$$

in which A_s is the cross-sectional area of steel tube, f_y is the yield stress of steel tube, A_c is the cross-sectional area of concrete, and f_c is the cross-sectional area of concrete.

Thickness of the steel tube was set as 4 mm, 5 mm, and 6 mm, respectively. Meanwhile, the heating temperature was selected as 300°C, 600°C, and 900°C, respectively. The duration of heating under different temperatures is set as 60 min, 90 min, and 120 min, as shown in Table 1. The cross-section of the column is directly welded by two rectangular (square) steel tubes according to the design dimensions. The 3D schematic of the specimen is shown in Figure 1. Figure 2 shows the detailed section size of the TCFST short columns. Each combination of TCFST columns requires two cover plates (100 mm^2).

2.2. Material Properties.
The concrete used in this experiment has a design strength of C40 which is mixed by manual and mixer. According to the "general concrete mix proportion design code" JGJ55-2011 specification [40], the concrete mix proportion is shown in Table 2. According to Chinese code "test method for mechanical properties of ordinary concrete" GB/T50081-2002 specification [41], standard cube test blocks (150 mm × 150 mm × 150 mm) were poured at the same time to test the compressive strength of concrete. After all the concrete specimens were prepared, they were put into the standard curing room for 28 days. 5000 kN electro-hydraulic servo pressure-shear testing machine was used for material characteristic test and the concrete test strength parameters are presented in Table 3. All specimens made by Q235 steel were used in this experiment, according to the recommendations of the Chinese code of metallic materials [42]; standard tensile coupons taken from each type of steel tube were tested to measure mechanical properties. Figure 3 shows the experimental process of standard tensile coupons, and the parameters of steel are given in Table 4.

Table 1: Summary table of experimental control parameters.

Specimen label	Thickness (mm)	Temperature (°C)	Time (h)
Th4T20t0	4	20	0
Th5T20t0	5	20	0
Th6T20t0	6	20	0
Th4T300t1.0	4	300	1.0
Th5T300t1.0	5	300	1.0
Th6T300t1.0	6	300	1.0
Th4T300t1.5	4	300	1.5
Th5T300t1.5	5	300	1.5
Th6T300t1.5	6	300	1.5
Th4T300t2.0	4	300	2.0
Th5T300t2.0	5	300	2.0
Th6T300t2.0	6	300	2.0
Th4T600t1.0	4	600	1.0
Th5T600t1.0	5	600	1.0
Th6T600t1.0	6	600	1.0
Th4T600t1.5	4	600	1.5
Th5T600t1.5	5	600	1.5
Th6T600t1.5	6	600	1.5
Th4T600t2.0	4	600	2.0
Th5T600t2.0	5	600	2.0
Th6T600t2.0	6	600	2.0
Th4T900t1.0	4	900	1.0
Th5T900t1.0	5	900	1.0
Th6T900t1.0	6	900	1.0
Th4T900t1.5	4	900	1.5
Th5T900t1.5	5	900	1.5
Th6T900t1.5	6	900	1.5
Th4T900t2.0	4	900	2.0
Th5T900t2.0	5	900	2.0
Th6T900t2.0	6	900	2.0

Note. Th, thickness; *T*, temperature; *t*, time.

Figure 1: 3D schematic of specimen.

Figure 2: Section diagram of the TCFST column.

Table 2: Concrete mix proportion.

Type	Cement	Water	Sand	Gravel	Water reducing agent
Proportion	1	0.39	1.29	2.88	0.01

Table 3: Experimenting strength of concrete.

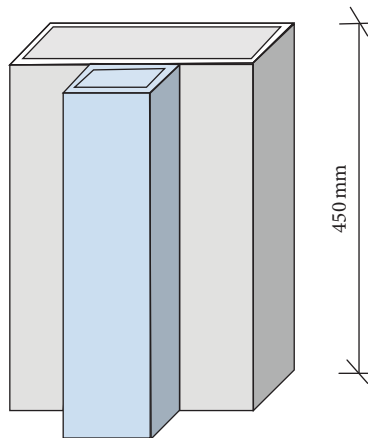| Label	Test strength (MPa)	Average value (MPa)
1	39.7	
2	40.3	40.2
3	40.6	

Figure 3: Test of steel standard specimen.

2.3. Elevated Temperature Design and Heating System.

As mentioned above, three temperature conditions were selected in this paper, including 300°C, 600°C, and 900°C. The elevation of the air temperature in the high-temperature electric furnace is monitored (the thermocouple is not arranged 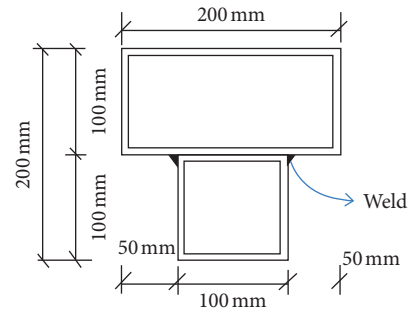inside the test piece and the only temperature in the furnace was controlled during the test); the time-temperature curve is obtained by equation (2). Then, when the heating temperature reached the specific temperature, the furnace kept the target temperature for 60 min, 90 min, and 120 min, respectively. Finally, specimens were naturally cooled to the room temperature after heating. The elevated temperature experimental furnace is depicted in Figure 4.

TABLE 4: Experimenting parameter of steel.

Steel tube size (mm)	Yield strength (MPa)	Elastic modulus (MPa)	Ultimate tensile strength (MPa)
$4 \times 100 \times 100$	291.58	2.0×10^5	418.54
$4 \times 100 \times 200$	305.23	1.95×10^5	419.88
$5 \times 100 \times 100$	300.23	2.01×10^5	381.47
$5 \times 100 \times 200$	306.57	1.96×10^5	383.24
$6 \times 100 \times 100$	312.21	1.93×10^5	387.87
$6 \times 100 \times 200$	308.53	2.01×10^5	393.68

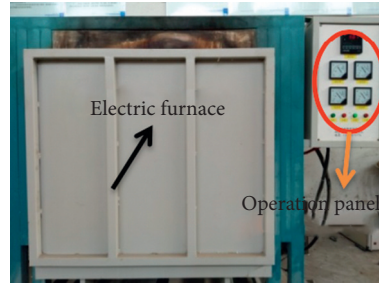
FIGURE 4: Elevated temperature experimental furnace.

$$\text{Warming section,} \, T = T_0 + 345 \log_{10}(8t + 1),$$

$$\text{Cooling section,} \quad T_c = \begin{cases} T - 10.417 (t_t - t) & t \leq 30 \, \text{min}, \\ T - 4.617 \left(3 - \dfrac{t_h}{60}\right)(t_t - t) & 30 \, \text{min} \leq t \leq 120 \, \text{min}, \\ T - 4.617 (t_t - t) & t > 120 \, \text{min}, \end{cases} \tag{2}$$

where T_0 is the room temperature (°C); t is the elevated temperature time (min); T_c is the cooling temperature (°C); t_t is the total operating time (min).

As described in Section 2.1, thirty specimens were divided into ten groups, nine of which were subjected to elevated temperature, and the remaining group is at the room temperature, which is used as a reference. The experimental phenomena of heating process are as follows:

The changes of steel and concrete can be observed during the heating process. When the temperature is 300°C, the performance of the steel tube is similar to that at the room temperature. After exposing to air, the color of steel tube is black slightly, and there are very few cracks in the concrete standard test block. When the temperature is 600°C, the phenomenon is similar, while the surface of the steel tube becomes darker during the cooling process. After cooling, the surface of the steel tube is brick red, and cracks on the concrete standard test block are obvious. When the temperature is 900°C, the surface of the steel tube is red and transparent, and there is a crisp sound. Then, the surface of the steel tube quickly turns black after exposing to air, and it becomes silvery white with a large amount of iron sheet off after cooling to room temperature. The concrete standard test block has evident cracks. The specimen after cooling is illustrated in Figure 5, and the specimen cooling process is depicted in Figure 6.

2.4. Experimental Axial Pressure Device and Loading System. After the specimen is naturally cooled to room temperature under high temperature, the axial compression load was carried out on a 5000 kN electro-hydraulic servo pressure-shear testing machine. Figure 7 shows the hydraulic testing machine and the operating system. The entire test process is shown in Table 5.

All specimens were subjected to strain tests to investigate the stress-strain relationship of specimens. A group of strain gauges were divided into transverse strain and longitudinal strain with the interval of 90° of orthogonal arrangement. The strain gauge was attached to the middle of each steel tube surface. Figure 8 shows the strain gauge arrangement. The specimen is placed at the central position of the loading platform to make the stress uniform. The test data of strain gauges were collected by the DH3816 automatic data acquisition system, as shown in Figure 9.

FIGURE 5: Some of the specimens after cooling.

FIGURE 6: Cooling process of the specimen.

FIGURE 7: Experimental axial compression device.

TABLE 5: Loading system.

Loading process	P1	P2	P3	P4
Loading method	Displacement	Force	Force	Displacement
Loading level	0.5 mm/min	$1/10P_U$	$1/20P_U$	0.5 mm/min

Note. (1) P1 is before the contact. P2 is the elastic stage. P3 is the elastic-plastic stage. P4 is the yielding or breaking stage. (2) $p_u = f_y \times A_S + f_c \times A_c$, where p_u is the ultimate bearing capacity, f_y is the yield stress of steel tube, f_c is the strength of concrete, A_S is the cross-sectional area of steel tube, and A_c is the cross-sectional area of concrete.

3. Experiment Results

3.1. Failure Modes. There are three typical failure modes under axial compression, which are local cracks, drum damage, and shear damage. As shown in Figure 10, there is only one of the specimens (specimen label: Th4T300t1.5) was found that the local cracks appeared on it, and the concrete at the crack crushed simultaneously. The test specimen first generated a drum in the big tube, while the small tube broke and thus cracked the test specimen suddenly. The cracks on the test specimen may be caused by the following reasons: (1) the phenomenon of stress concentration occurs at the corner of the small steel tube column; (2) the steel tube outside the small steel tube column has poor forming quality. Figure 11 shows the phenomenon of drum damage on the specimens; the concrete at the damaged
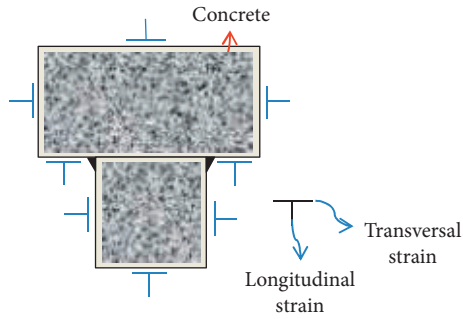
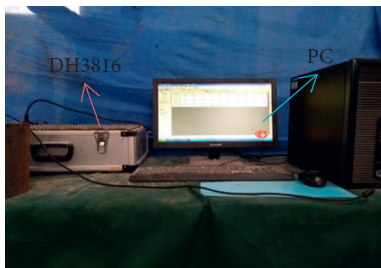FIGURE 8: Schematic layout of strain gauges.

FIGURE 9: Data acquisition system.

FIGURE 11: Drum damage.
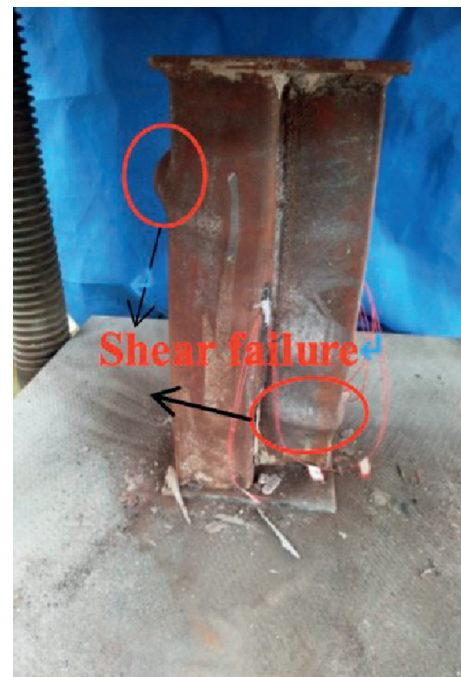

FIGURE 10: Local cracks.

FIGURE 12: Shear failure.

part was crushed. When the specimen was damaged due to bulge, the specimen usually formed three stories that are upper (upper end or 1/3 from the upper end), middle, and lower (lower end or 1/3 from the lower end). Because being greatly affected by the width-to-thickness ratio of the steel pipe, the sequence of the drumming follows the characteristics of big tube first and then small tube. Shear damages appear in a few specimens, as shown in Figure 12, and the main phenomenon is that the big tube has a slip line, and the drum is at a certain angle. The reason of the shear damages on the test specimen may be caused by that the web of the big tube has a large radius of gyration due to the large width. So, when the axial load was applied to a certain value, the steel pipe wall of the big tube formed a shear slip line. With the axial load increased, the big tube of the test piece was bulged along the slip line and subsequently destroyed.

3.2. Load-Strain Curve. The trend of strain changes in the TCFST short columns is measured by the DH3816 automatic data acquisition system. The load-strain curves of all specimens are shown in Figure 13. Subfigures 1, 3, 5, 7, and 9 represent the longitudinal strains and 2, 4, 6, 8, and 10 represent the transversal strains. Due to the symmetry of TCFST, the average value is used to draw load-strain curves.

According to Figure 13, it can be seen that the strain of the specimen increases linearly with the increase of the axial load. Under the load when the T-shaped CFST short column is in the elastic stage, the deformation of the specimen is consistent under the axial load, and the cross-section stress distribution of the specimen is more uniform; when the T-shaped concrete-filled steel tube short column enters into the elastic-plastic stage and the plastic stage, the strain value suddenly increases. At this time, the specimen began to appear like drum bending phenomenon. The change of strain reflected that the change of specimen was consistent with the experimental phenomenon. At the same time, it can be seen from some drawings that the strain change of some sections is abnormal. The reason may be that the concrete pouring is not good, and the strain gauge of these sections does not achieve the ideal bonding effect. Overall, the change of strain shows that the change of curve is consistent with the experimental phenomenon.

4. Analysis of Test Results

In the elastic phase, the curve increases almost linearly. The axial load of the specimen grows faster, while the vertical displacement of the specimen increases slowly. In the elastoplastic stage, the axial load of the specimen increases slowly while the vertical displacement increases rapidly. In the plastic phase, the load-displacement curve is almost horizontal, and the axial load of the test piece remains unchanged while the vertical load increases rapidly. Finally, in the failure stage, the specimens began to suffer from drumming failure and the bearing capacity decreased rapidly.

4.1. Effect of Temperature. The load-displacement curve can reflect the path trajectory of the structural member's bearing capacity change from the starting to the ending of the axial load. The axial load (P) and deformation (Δ) curves of the TCFST short column that have different temperatures, same steel ratio, and heating duration are compared in Figure 14. The label "4-300-1" indicates that the steel tube thickness is 4 mm, the temperature is 300°C, and the duration is 1 hour (60 min).

It can be seen from Figure 14 that the displacement load curves of all specimens are composed of three stages (elastic stage, elastoplastic stage, and plastic stage). In the elastic stage, the curve rises linearly before the inflection point of the curve. At this stage, the axial load increases rapidly, while the vertical displacement increases slowly. In the elastic-plastic stage, the axial load increases slowly after the inflection point of the curve, but the vertical displacement increases faster. In the plastic stage, the load-displacement curve is almost parallel to the coordinate axis. In this stage, the axial load of the specimen remains unchanged, but the vertical load increases rapidly. With the increase of temperature, the elastic section of the specimen decreases gradually, the elastic-plastic stage is prolonged, and the yield strength reaches earlier. The displacement load curves of 300°C and 600°C specimens have little difference of curves shape, but the displacement loads of 900°C specimens are different from those of other temperatures, which is because the internal core concrete of the specimens at 300°C and 600°C were still working, but the core concrete in the specimens at 900°C were basically in a failure state. After cutting the specimen under axial compression, the core concrete in the specimen at 900°C was basically scattered and in sand shape. As shown in Figure 14, when the high temperature lasts for 1 hour, the displacement load curves of 300°C and 600°C specimens basically coincide, but the displacement load of 900°C specimens has obvious changes; when the high temperature continues for 1.5 hours, the displacement load curves of 300°C, 600°C, and 900°C specimens have a downward trend; when the high temperature lasts for 2 hours, the displacement load curves of 300°C, 600°C, and 900°C specimens have a downward trend. In general, with the increase of temperature, the stiffness of the specimens is in a degradation state, and the ductility performance is getting better.

4.2. Effect of Heating Duration. The axial load (P) and deformation (Δ) curves of the TCFST column that have different heating duration and the same steel ratio and temperature are compared in Figure 15.

From Figure 15, it can be seen that the trends of load-displacement curves of all the experiment specimens are almost the same. The initial stiffness of the steel tube with the same temperature and different heating duration is almost the same in the elastic stage (i.e., the slope of the load-displacement curve in the elastic stage), which indicates that the initial stiffness of the elastic stage specimen is not affected by the duration. As the duration increases, the elastic section of the specimen does not increase or decrease significantly, and the elastic-plastic section does not change significantly. The specimens show toughness at 900°C, since the high temperature eliminates the internal stress in the hardened steel. It can be seen from the load-displacement curves that the duration has little effect on the bearing capacity of TCFST short columns.

4.3. Effect of Steel Tube Thickness. The axial load (P) and deformation (Δ) curves of the TCFST short column that have different steel tube thicknesses and the same temperatures and heating duration are compared in Figure 16.
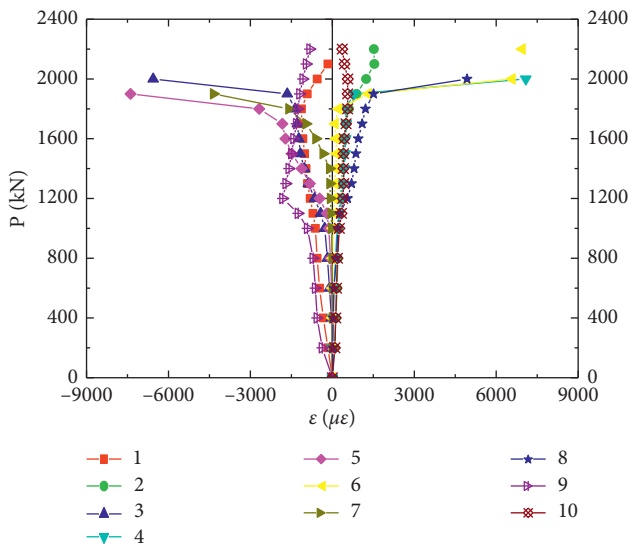
It can be seen from Figure 16 that the displacement load curves of all experiment specimens are almost the same in the elastic stage. At the same time, we can also see that the changing trend is consistent after the experiment specimens enter the elastoplastic stage. With the increase of wall
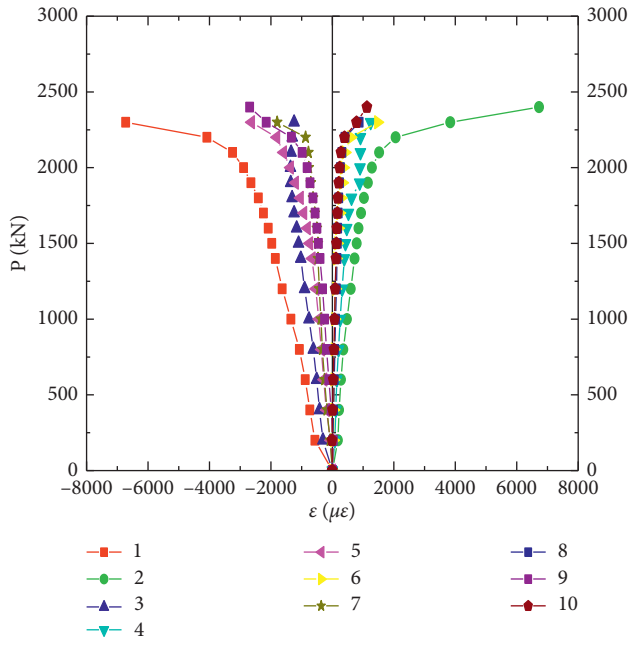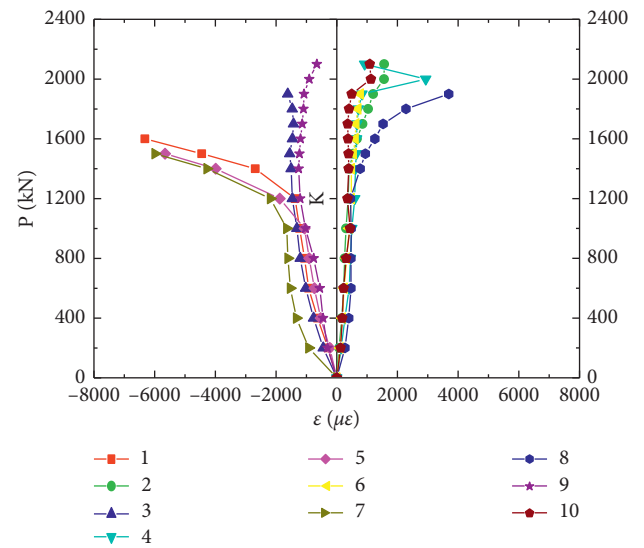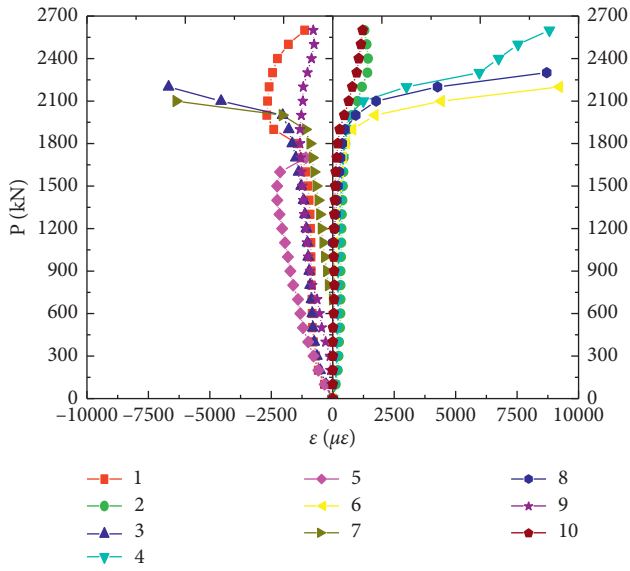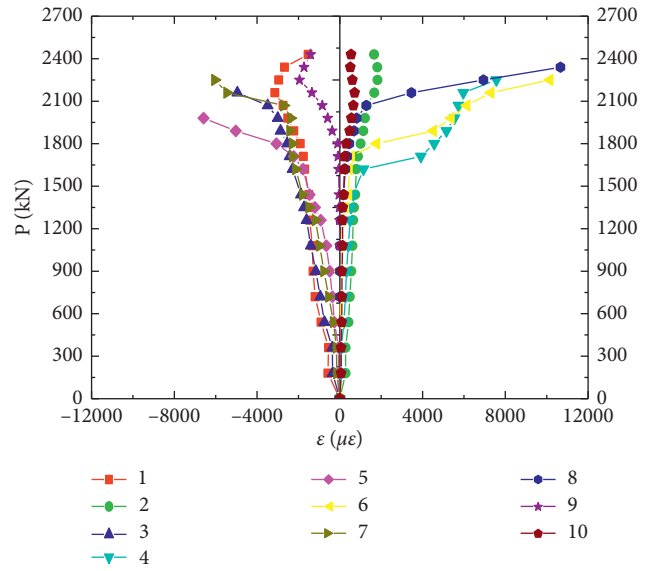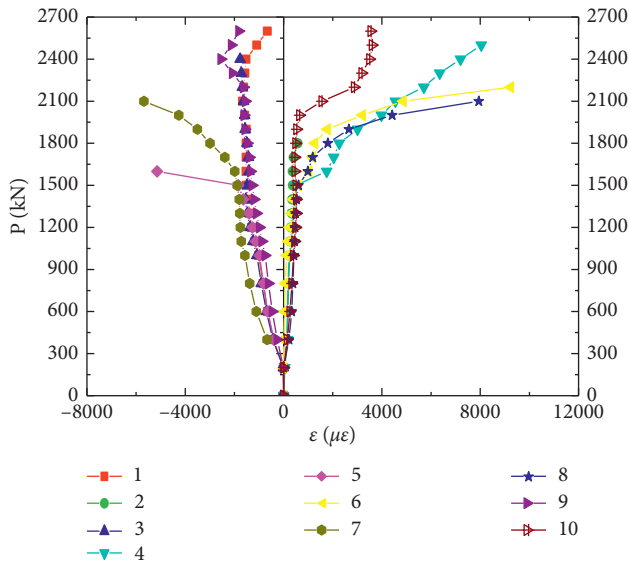
(a)
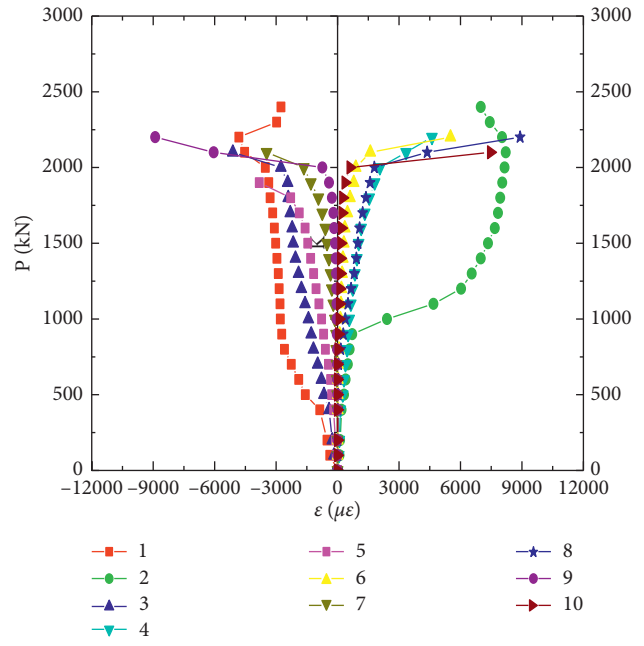
(b)

(c)

(d)

FIGURE 13: Continued.

(e)

(f)

(g)

(h)

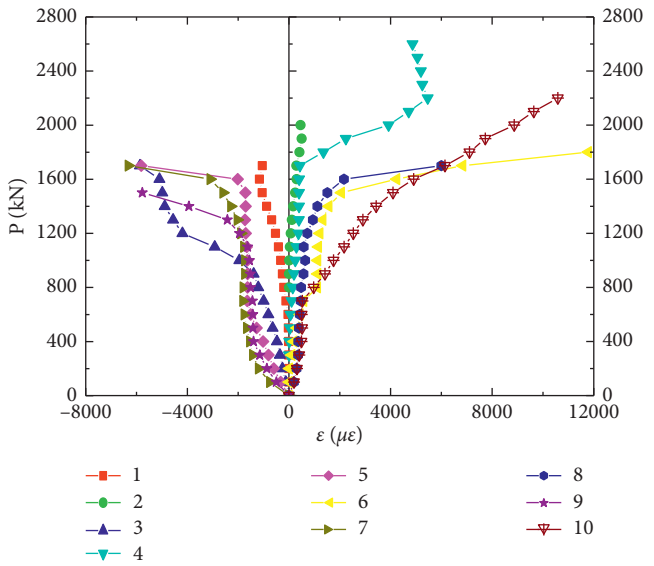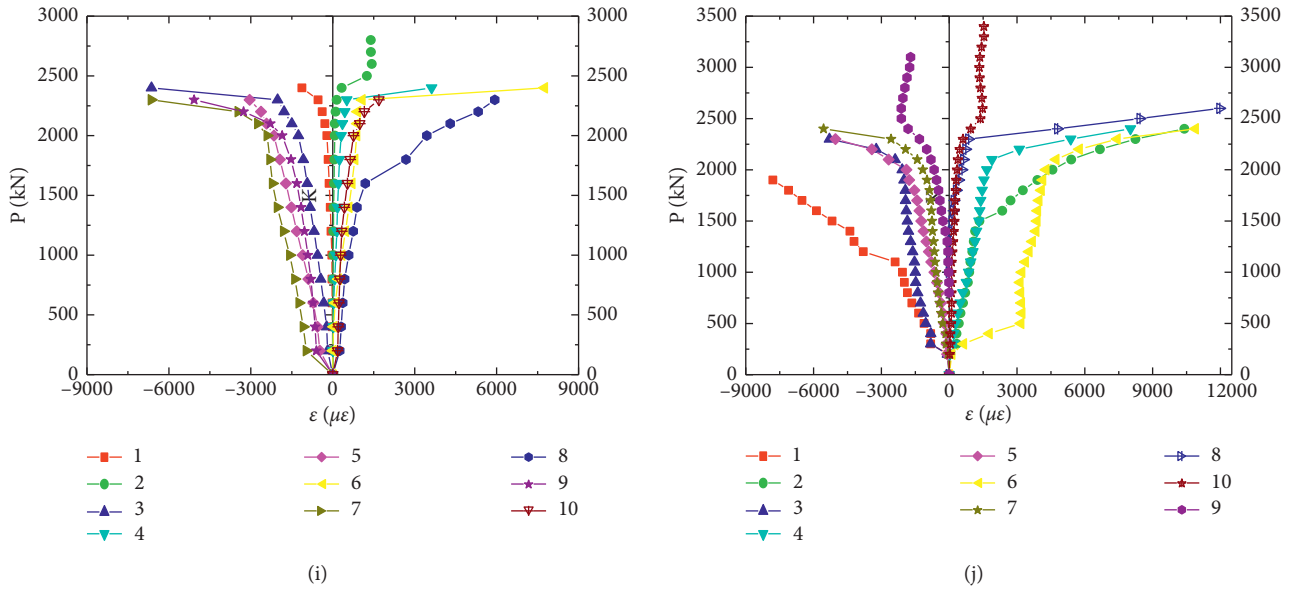FIGURE 13: Continued.

(i)

(j)

Figure 13: Load-strain curves of some specimens at 300 and 600. (a) 4 mm-300°C-1 hour. (b) 4 mm-300°C-1.5 hours. (c) 4 mm-600°C-1 hour. (d) 4 mm-600°C-2 hours. (e) 5 mm-300°C-1 hour. (f) 5 mm-300°C-2 hours. (g) 5 mm-600°C-1 hour. (h) 6 mm-600°C-1 hour. (i) 6 mm-300°C-1 hour. (j) 6 mm-300°C-2 hours.

(a)

(b)

(c)

(d)

(e)

(f)
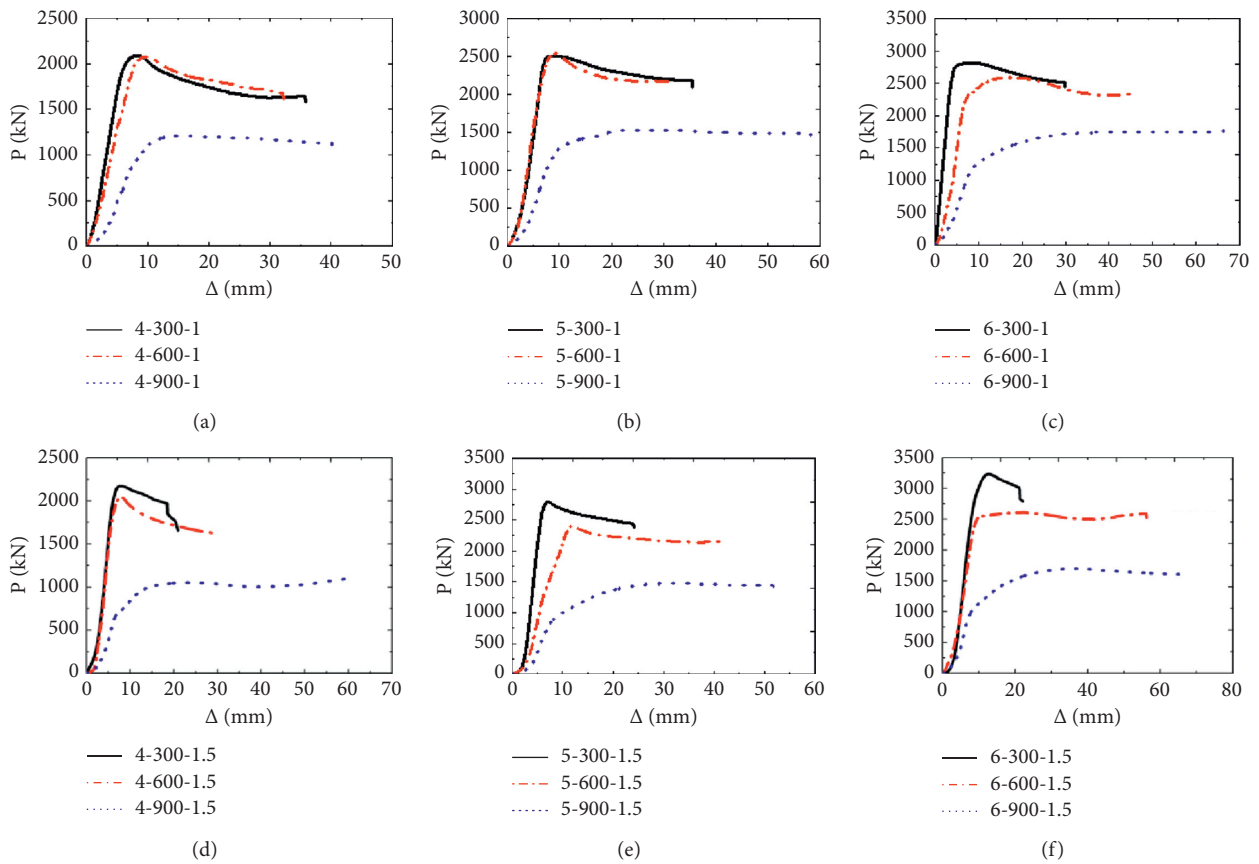
Figure 14: Continued.

(g)

(h)

(i)
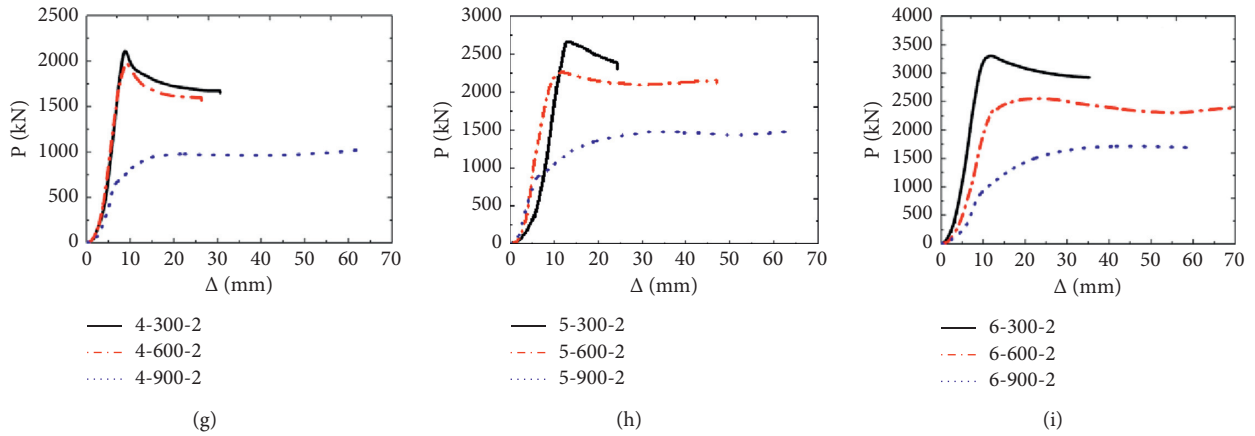
FIGURE 14: Different temperatures for the same duration and the same steel ratio. (a) 4 mm thickness with 1 hour heating. (b) 5 mm thickness with 1 hour heating. (c) 6 mm thickness with 1 hour heating. (d) 4 mm thickness with 1.5 hours heating. (e) 5 mm thickness with 1.5 hours heating. (f) 6 mm thickness with 1.5 hours heating. (g) 4 mm thickness with 2 hours heating. (h) 5 mm thickness with 2 hours heating. (i) 6 mm thickness with 2 hours heating.

(a)

(b)

(c)

(d)

(e)

(f)
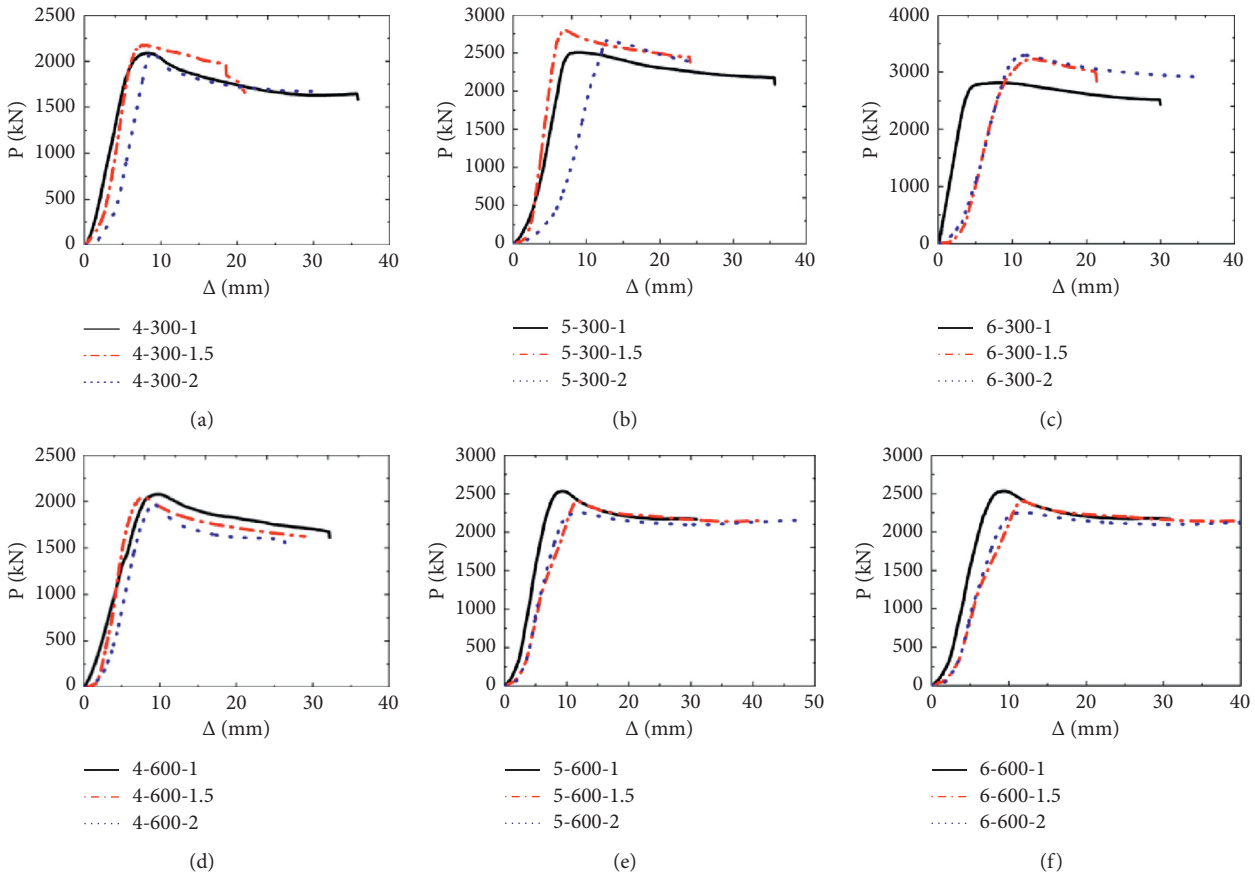
FIGURE 15: Continued.

(g)

(h)

(i)
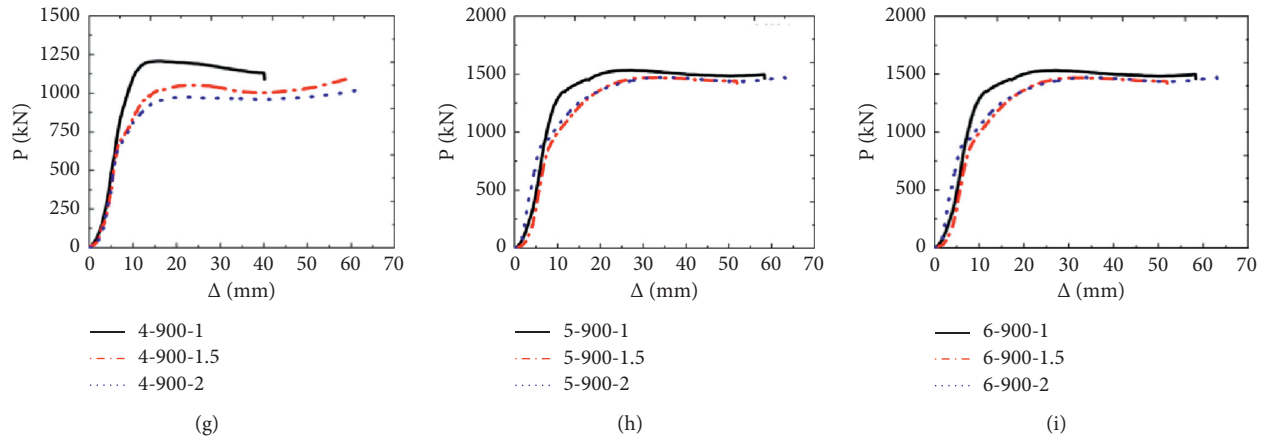
FIGURE 15: Different durations for the same wall thickness and the same temperature. (a) 4 mm thickness with 300°C temperature. (b) 5 mm thickness with 300°C temperature. (c) 6 mm thickness with 300°C temperature. (d) 4 mm thickness with 600°C temperature. (e) 5 mm thickness with 600°C temperature. (f) 6 mm thickness with 600°C temperature. (g) 4 mm thickness with 900°C temperature. (h) 5 mm thickness with 900°C temperature. (i) 6 mm thickness with 900°C temperature.

(a)

(b)

(c)

(d)

(e)

(f)
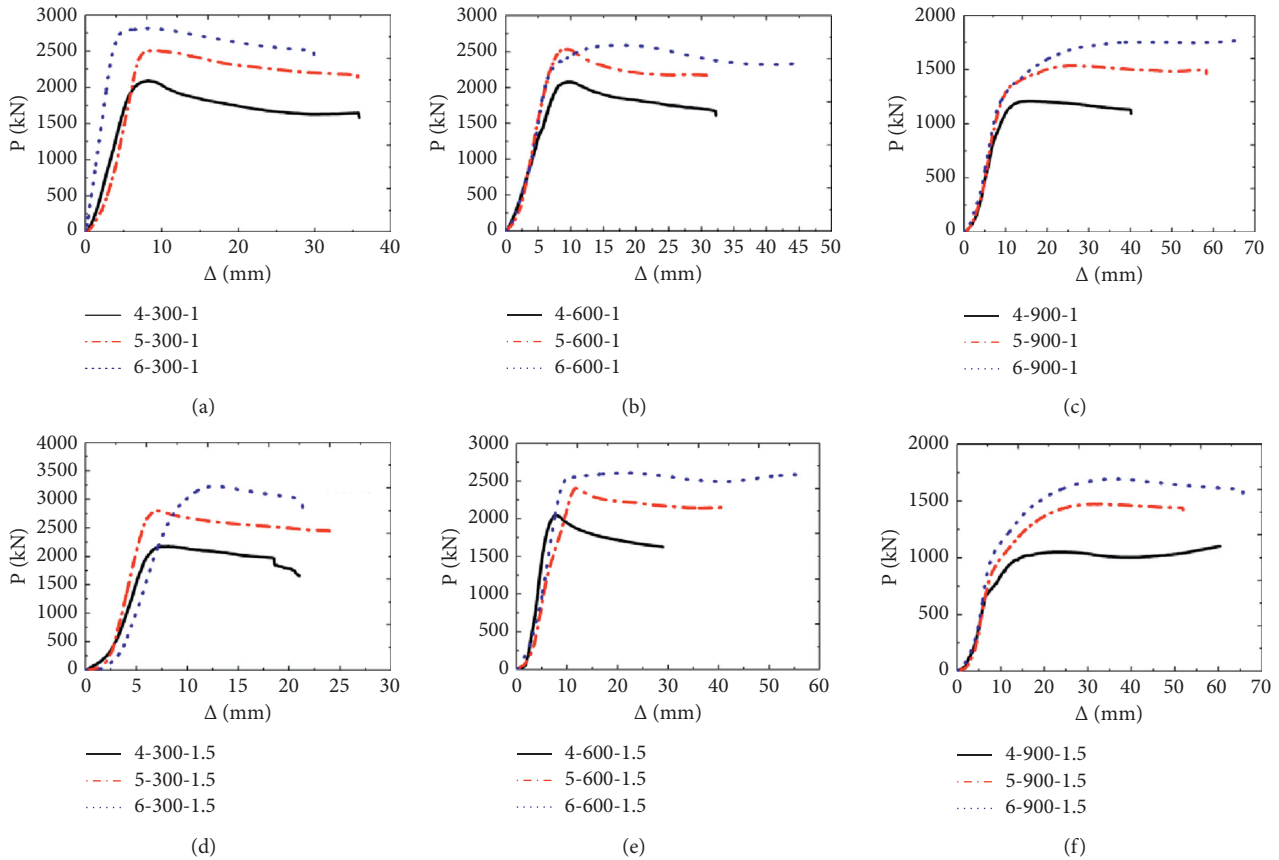
FIGURE 16: Continued.

(g)   (h)   (i)
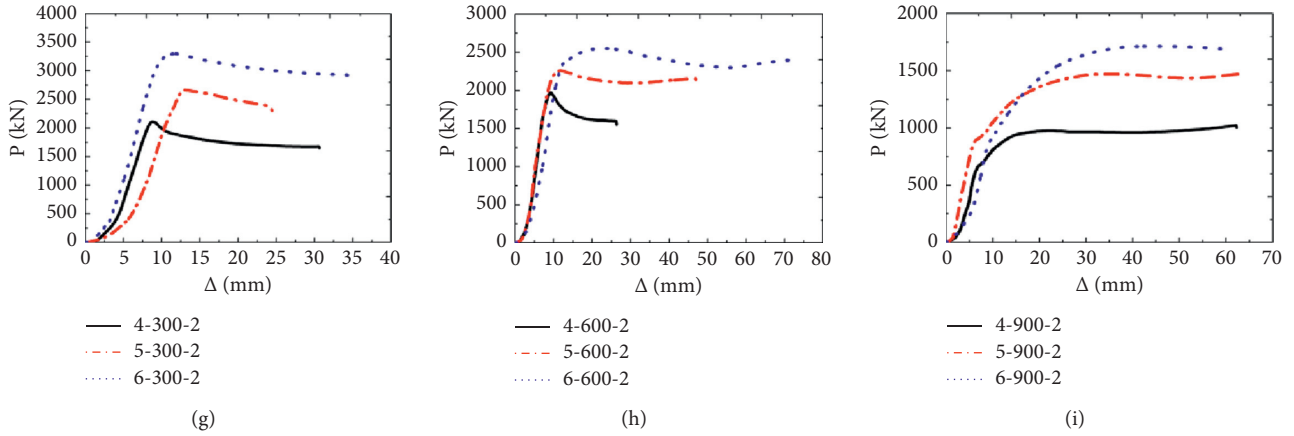
FIGURE 16: Different wall thicknesses for the same heating duration and temperature. (a) 300°C temperature with 1 hour heating. (b) 600°C temperature with 1 hour heating. (c) 900°C temperature with 1 hour heating. (d) 300°C temperature with 1.5 hours heating. (e) 600°C temperature with 1.5 hours heating. (f) 900°C temperature with 1.5 hours heating. (g) 300°C temperature with 2 hours heating. (h) 600°C temperature with 2 hours heating. (i) 900°C temperature with 2 hours heating.

thickness, the initial stiffness of the specimen in the elastic phase increases continuously. When the temperature and duration are constant, the ultimate bearing capacity increases with the increasing steel ratio. It can be seen from the load-displacement curve that the thickness of steel tube has a great influence on the bearing capacity of TCFST short column.

5. Ultimate Bearing Capacity

There are three experimental parameters in this paper, i.e., the temperature, the duration, and the steel ratio. Therefore, the relationship between the ultimate bearing capacity and each parameter should be studied. Compared to the experiment specimens under the room temperature, the bearing capacity of most experiment specimens under the design parameters decreased. The temperature (T), the steel ratio (α), and the duration of heating (t) are the factors that can be used to conduct curve fitting to obtain the following equation as

$$N = N_u f(\alpha, t, T), \tag{3}$$

where $f(\alpha, t, T)$ is a regression fit relationship; $N_u = f_y A_s + 1.4 f_{ck} A_c$ is the intensity reference value at room temperature [43]; $\alpha = A_s f_y / A_c f_c$ is the steel ratio, which is controlled by the wall thickness of the steel tube; t is the time with the unit of min; and T is temperature with the unit of °C.

A simplified formula was proposed to determine the ultimate bearing capacity of TCFST short columns under axial compressive load after elevated temperature, as given by the following equation, and the data fitting results with errors are shown in Table 6.

$$f = -0.12 + 10.95\alpha + 0.001t + 0.0015T - 32.17\alpha^2$$
$$- 1.36 \times 10^{-6} t^2 - 2.86 \times 10^{-6} tT. \tag{4}$$

6. Finite Element Numerical Simulation

The finite element program ABAQUS was used for numerical analysis of CFST columns after elevated temperature under axial compression. Finite element analysis was mainly used for digital simulation and verification of experimental results. Firstly, the appropriate constitutive relation of steel and core concrete after elevated temperature was selected, and then the parameter adjustment method was used to establish the mechanical analysis model of T-shaped concrete-filled steel tubular short column after elevated temperature. The ultimate bearing capacity, failure modes, and load-displacement curves obtained from FEA models were compared with the experimental test data.

6.1. Constitutive Relation of Materials. At the ambient temperature, this section uses a five-stage elastoplastic model to characterize the stress-strain relationship of the steel tube. As depicted in Figure 17, this model is composed of the elasticity (oa), the elastic plasticity (ab), the plasticity (bc), the strengthening (cd), and the secondary plastic flow (de) phase [44], and corresponding formulas of the stress-strain curve under each phase are presented in equation (4). The solid line denotes the simplified stress-strain relationship curve of the steel, and the red line represents the actual stress-strain relationship curve of the steel.

$$\sigma = \begin{cases} E_s \varepsilon_s, \\ -A\varepsilon_s^2 + B\varepsilon_s + C, \\ f_y, \\ f_y \left[1 + 0.6 \dfrac{\varepsilon_s - \varepsilon_{e2}}{\varepsilon_{e3} - \varepsilon_{e2}} \right], \\ 1.6 f_y, \end{cases} \tag{5}$$

TABLE 6: Fitting analysis of ultimate bearing capacity of specimens.

| Experiment specimens' number	Ultimate bearing capacity experimental value N1 (kN)	Fitting predicted value N2 (kN)	Difference N2-N1 (kN)	Percentage error
4-20-0	2307.8			
4-300-1.0	2165.2	2306.29	141.09	6.52%
4-600-1.0	2141.2	2111.33	−29.87	−1.40%
4-900-1.0	1259.6	1316.34	56.74	4.50%
4-300-1.5	2241.2	2371.51	130.31	5.81%
4-600-1.5	2072.2	2137.92	65.72	3.17%
4-900-1.5	1122.6	1214.30	91.70	8.17%
4-300-2.0	2144.8	2336.73	191.93	8.95%
4-600-2.0	1997.0	2164.50	167.50	8.39%
4-900-2.0	1048.0	1152.25	104.25	9.95%
5-20-0	2670.4			
5-300-1.0	2610.2	2798.49	188.29	7.21%
5-600-1.0	2608.6	2572.90	−35.70	−1.37%
5-900-1.0	1586.4	1722.43	136.03	8.57%
5-300-1.5	2838.8	2873.96	35.16	1.24%
5-600-1.5	2434.4	2603.66	169.26	6.95%
5-900-1.5	1497.2	1608.49	111.29	7.43%
5-300-2.0	2699.4	2949.42	250.02	9.26%
5-600-2.0	2292.0	2434.42	142.42	6.21%
5-900-2.0	1504.6	1664.55	159.95	10.63%
6-20-0	3120.2			
6-300-1.0	2816.0	3040.90	224.90	7.99%
6-600-1.0	2728.8	2977.30	248.50	9.11%
6-900-1.0	1857.4	1983.58	126.18	6.79%
6-300-1.5	3256.0	3329.08	73.08	2.24%
6-600-1.5	2684.8	2913.25	228.45	8.51%
6-900-1.5	1724.8	1867.30	142.50	8.26%
6-300-2.0	3328.4	3417.25	88.85	2.67%
6-600-2.0	2582.6	2749.19	166.59	6.45%
6-900-2.0	1753.2	1951.01	197.81	11.28%
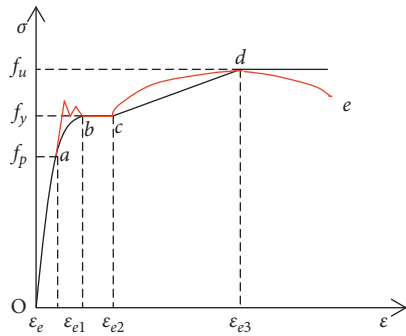
FIGURE 17: Stress-strain curve of steel.

where E_s is the elastic modulus of steel; $A = 0.2 f_y / \varepsilon_{e_1} - \varepsilon_e$; $B = 2 A \varepsilon_{e1}$; $C = 0.8 f_y + A \varepsilon_e^2 - B \varepsilon_e$; $\varepsilon_e = 0.8 f_y / E_s$; $\varepsilon_{e1} = 1.5 \varepsilon_e$; $\varepsilon_{e2} = 10 \varepsilon_e$; and $\varepsilon_{e3} = 100 \varepsilon_e$.

The constitutive relationship model of the steel under elevated temperature still uses the five-stage elastoplastic model of the steel at room temperature. Since the steel material has experienced elevated temperature, its elastic modulus and yield strength are adjusted according to the highest temperature experienced by the steel. Moreover, the stress-strain relationship of the structural material model of the steel after the elevated temperature is adjusted, as shown in the following equation:

$$\sigma = \begin{cases} E_s(T_{max}) \cdot \varepsilon, \\ f_y(T_{max}) + E_s'(T_{max})[\varepsilon - \varepsilon_s(T_{max})], \end{cases} \quad (6)$$

where T_{max} is the highest temperature experienced by the steel; $E_s(T_{max})$ is the elastic modulus of the steel after elevated temperature; $E_s'(T_{max}) = 0.01 E_s(T_{max})$ is the elastic modulus of the steel in the strengthening stage after elevated temperature; $f_y(T_{max})$ is the yield strength of the steel after elevated temperature; and $\varepsilon_s(T_{max})$ is the yield strain of the steel after elevated temperature.

The commonly used stress-strain relationship of the concrete may be different from the actual situation of the TCFST structure. Thus, we considered the constraint effect of steel tube on the concrete by employing Han's model [1]. The specific expression of the model is presented in equation (7). The tensile stress-strain relationship is expressed by the relationship between the uniaxial tensile stress and strain of concrete proposed in prior investigation [45]. The specific

expression of the model is presented in equation (8). The selection of the concrete damage model is based on the damage model of Lee et al. [46].

$$y = \begin{cases} 2x - x^2, & x \leq 1, \\ \dfrac{x}{\beta_0 (x-1)^\eta + x}, & x > 1, \end{cases} \quad (7)$$

where $x = \varepsilon/\varepsilon_0$; $y = \sigma/\sigma_0$; $\sigma_0 = f_c$ is the peak stress of the concrete stress; f_c represents the compressive strength of the concrete cylinder; $\varepsilon_0 = \varepsilon_{cc} + 800 \cdot \xi^{0.2} \cdot 10^{-6}$ is the concrete peak compressive strain; $\xi = A_s f_y / A_c f_{ck}$ is the constraint effect coefficient; A_s is the cross-sectional area of the steel tube; A_c is the cross-sectional area of the concrete; f_y is the yield strength of the steel; f_{ck} is the standard value of concrete axial compressive strength; $\varepsilon_{cc} = (1300 + 12.5 \cdot f_c) \cdot 10^{-6}$; $\eta = 1.6 + 1.5/x$; and $\beta_0 = f_c^{0.1}/(1.2 \cdot \sqrt{1 + \xi})$.

$$y = \begin{cases} 1.2x - 0.2x^6, & x \leq 1, \\ \dfrac{x}{\alpha_i (x-1)^{1.7} + x}, & x > 1, \end{cases} \quad (8)$$

where $\alpha_i = 0.312\sigma_p^2$; $x = \varepsilon/\varepsilon_p$; $y = \sigma/\sigma_p$; $\varepsilon_p = 43.1\sigma_p (\mu\varepsilon)$ is the strain corresponding to the peak compressive stress; and $\sigma_p = 0.26 \cdot (1.25 f_c)^{2/3}$ is the peak compressive stress.

6.2. FEA Models.

In the FEA model, shell elements were used to simulate steel tubes, and solid elements were used to simulate concrete and cover plate. There was no relative sliding between steel pipes; the surface to surface contact between steel pipes and concrete allowed relative sliding; the cover plates on both sides and steel pipes were consolidated to ensure that the steel pipes and cover plates were not separated during loading; it is assumed that the section of the concrete-filled steel pipe remains flat during loading; the material defects caused by welding and the elevated temperature were not considered; the coordination relationship between longitudinal balance and deformation was considered in the model. In the process of simulation analysis, the bottom of the column is a fixed end. After elevated temperature, axial compression is carried out, and a limit displacement was applied at the geometric center point of the T-section at the top of the column. The typical finite element mesh of SHST columns is shown in Figure 18.

6.3. Validation of FEM

6.3.1. Failure Mode.

The failure mode of most of the specimens in the experiment is similar to that obtained via the finite element simulation, and they both show the drum phenomenon. A comparison between the numerical damage and the experimental damage is depicted in Figure 19.

6.3.2. Load-Displacement Curves.

Now select the representative test pieces under each specimen, draw the experimental load-displacement curve in Figure 20, and simulate the load-displacement curves corresponding to the output of the finite element through the finite element method. In the finite element simulation, output the displacement of the loading displacement point and the vertical reaction of the bottom endplate reaction output point and obtain the curve relationship between the load of the test piece and the longitudinal displacement as shown in Figure 21. It can be seen from Figures 20 and 21 that, compared with the experimental load-displacement curve, when the peak load is reached, the displacement corresponding to the finite element simulation output is generally smaller than the displacement corresponding to the actual experiment, and the limit load obtained by the finite element is generally larger than the actual experimental limit load, but the overall trend is basically the same. It should be noted that differences in the shape of the P-delta curves of TH6T900T2.0 specimen were obtained experimentally and numerically. The possible reason is that during the loading process of the test specimen, the test machine stopped loading due to the oil pressure fault, so the test was suspended and the specimen was unloaded for the maintenance of the machine. Tests on the specimen were resumed when the instrument returned to normal. The process of loading, unloading, and secondary loading probably improves the plasticity of the specimen, which in turn leads to the difference from the finite element analysis.

6.3.3. The Ultimate Bearing Capacity.

After modeling, the output software calculates the ultimate bearing capacity of each test piece and records it as shown in Table 7. By comparing the ultimate bearing capacity collected from the test with the ultimate bearing capacity output from the finite element, we can judge whether the established model is reliable by comparing the difference between the two and judge whether the reduction treatment of the model for each material is feasible.

The ultimate bearing capacity obtained by the finite element method is generally higher than the ultimate bearing capacity measured by the actual experiment. The main reasons are as follows: the properties of materials change greatly after elevated temperature, especially the internal concrete. After experiencing 900 degrees high temperature, the experimental situation was a state of crushing as soon as pressing, especially the cohesive force and friction force between the sand and the stone inside the concrete were majorly lost, but in the finite element simulation, although the material is reduced, it still had a certain degree of expansion, which was quite different from the actual situation, so the bearing capacity in the finite element was generally greater than the actual test results, but the general situation can reflect the stress state.
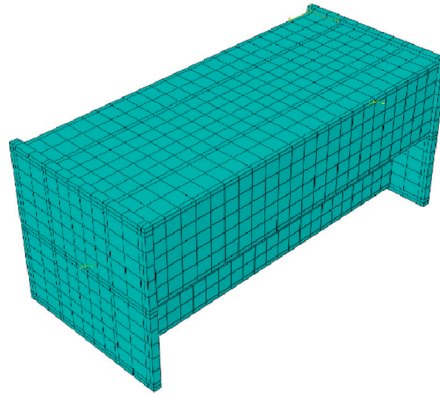
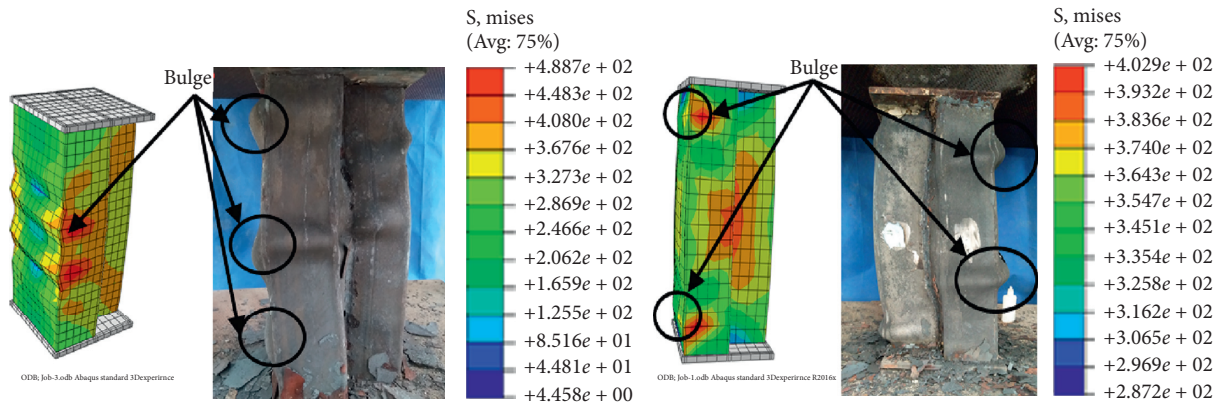FIGURE 18: Typical finite element mesh of CFST stub columns.

FIGURE 19: Comparison between FEA results and experimental values.
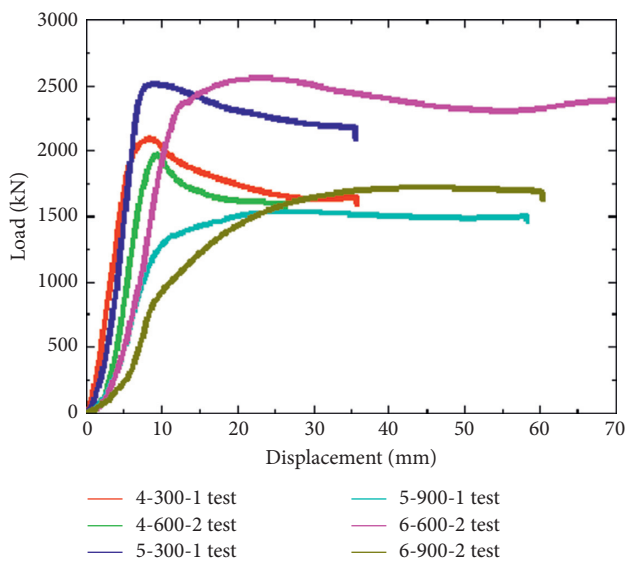

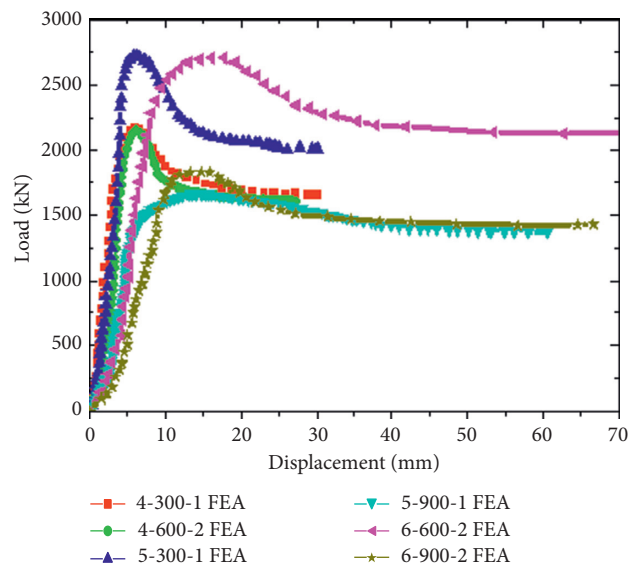FIGURE 20: Load-displacement curve of the specimen.

FIGURE 21: Load-displacement curve of FEA.

Table 7: Comparisons of ultimate bearing capacity and finite element bearing capacity.

Experiment specimens' number	Experimental values (kN)	Finite element (kN)	Difference value (kN)	Percentage error (%)
4-0-20	2307.8			
4-1.0-300	2165.2	2237.30	72.10	3 .33
4-1.0-600	2141.2	2286.37	145.17	6.78
4-1.0-900	1259.6	1416.80	157.20	12.48
4-1.5-300	2241.2	2347.21	106.01	4.73
4-1.5-600	2072.2	2179.13	106.93	5.16
4-1.5-900	1122.6	1261.47	138.87	12.37
4-2.0-300	2144.8	2301.16	156.36	7.29
4-2.0-600	1997.0	2218.27	221.27	11.08
4-2.0-900	1048.0	1193.78	145.78	13.91
5-0-20	2670.4			
5-1.0-300	2610.2	2864.96	254.76	9.76
5-1.0-600	2608.6	2914.85	306.25	11.74
5-1.0-900	1586.4	1881.63	295.23	18.61
5-1.5-300	2838.8	3252.98	414.18	14.59
5-1.5-600	2434.4	2636.70	202.30	8.31
5-1.5-900	1497.2	1757.41	260.21	17.38
5-2.0-300	2699.4	3057.61	358.21	13.27
5-2.0-600	2292.0	2517.07	225.07	9.82
5-2.0-900	1504.6	1800.55	295.95	19.67
6-0-20	3120.2			
6-1.0-300	2816.0	3073.95	257.95	9.16
6-1.0-600	2728.8	2959.93	231.13	8.47
6-1.0-900	1857.4	2015.65	158.25	8.52
6-1.5-300	3256.0	3519.08	263.08	8.08
6-1.5-600	2684.8	2844.55	159.75	5.95
6-1.5-900	1724.8	1878.82	154.02	8.93
6-2.0-300	3328.4	3607.32	278.92	8.38
6-2.0-600	2582.6	2723.87	141.27	5.47
6-2.0-900	1753.2	1890.65	137.45	7.84

7. Conclusions

This paper presents an experimental study and parametric analysis of axial compression of CFST column after elevated temperature. Based on the experimental results and the finite element simulation in this paper, the following conclusions are drawn:

(1) After the elevated temperature, the two square steel tubes of the TCFST short column have deformation consistency, and the overall force is uniform. The failure modes consist of the local crack, drum-shaped damage, and shear failure.

(2) Based on the load-displacement curve analyses, the ultimate bearing capacity of the specimen gradually decreases with the increase of temperature under the same heating duration. Particularly, the bearing capacity reduces more severely with higher temperature. Meanwhile, the ultimate bearing capacity of the experiment specimens will increase with a thicker wall.

(3) The initial stiffness of the specimens with the same temperature and heating duration in the elastic phase (the slope of the load-displacement curve in the elastic phase) is almost the same, indicating that the duration has no significant effect on the initial stiffness in the elastic phase. The load-displacement curves of the specimens with the same temperature

and different durations are consistent. With the increasing of heating duration, the elastic section of the specimen keeps constant, and the elastic-plastic section does not change significantly. The descending sections and the ductility are almost the same, which demonstrates that different heating duration has no significant effect on the ductility of the specimen.

(4) In the elastic stage of the TCFST short column, the strain of specimens increases linearly with the increasing of the axial load. The deformation of experiment specimens remains constant under the axial load, and the cross-sectional stress distribution is also uniform. When the TCFST short column enters the elastoplastic stage and the plastic stage, the strain value increases suddenly. At this time, the experiment specimens cause drum-shaped damages.

(5) A finite element model was developed through ABAQUS to simulate the failure modes of the TCFST short columns under axial compression after elevated temperature. Compared to the experimental failure modes, the results show that the finite element model is in good agreement with the experiment.

In this paper, due to limited experimental conditions, the distributed method is used to conduct experiments and simulation, and the discussion on the thermal coupling is

not sufficient. It is necessary to consider the thermal coupling effect to further enhance the development of special-shaped columns. This investigation only employed static loading, and the mechanism of action under coupling between dynamic load and thermal force will be investigated in the future work. Moreover, considering the efficiency of the piezo-enabled structural health monitoring method [47, 48] and percussion method [49] in detecting structural damages, we will apply these approaches to identify the damages in the TCFST in the future.

Nomenclature

T_0:	Room temperature
t:	Elevated temperature time
T_c:	Cooling temperature
t_t:	Total operating time
P:	Axial load
Δ:	Deformation
ε:	Average strain
$\mu\varepsilon$:	Unit of strain
T:	Temperature
$\alpha = A_s f_y / A_c f_c$:	Steel ratio
A_s:	Cross-sectional area of steel tube
f_y:	Yield stress of steel tube
A_c:	Cross-sectional area of concrete
f_c:	Compressive strength of standard concrete cubes
$\alpha_i = 0.312\sigma_p^2$:	Coefficient
$N_u = f_y A_s + 1.4 f_{ck} A_c$:	Intensity reference value at room temperature
f_{ck}:	Characteristic strength of concrete
E_s:	Elastic modulus of steel
$T_{\max}$:	Highest temperature experienced by the steel
$E_s(T_{\max})$:	Elastic modulus of the steel after elevated temperature
$E_s'(T_{\max})$:	Elastic modulus of the steel in the strengthening stage after elevated temperature
$f_y(T_{\max})$:	Yield strength of the steel after elevated temperature
$\varepsilon_s(T_{\max})$:	Yield strain of the steel after elevated temperature
σ_0:	Peak stress of the concrete stress
ε_0:	Concrete peak compressive strain
ξ:	Constraint effect coefficient
σ_p:	Peak compressive stress.

Data Availability

The data are real and reliable in this paper, including original experimental data and software analysis data. The data used to support the findings of this study are available from the corresponding author upon request.

Conflicts of Interest

The authors declare that they have no conflicts of interest.

Authors' Contributions

X. L., J. Z., and H. L. conceived the idea of this research. X. L., J. X., and J. Z. conducted the experiments. Y. R. and F. Y. analyzed the experiment data. X. L. and J. Z. wrote the paper. J. Z. and H. L. proofread and revised the paper.

Acknowledgments

References

[1] L. H. Han, *Concrete-filled Steel Tubular Structure-Theory and Practice* pp. 1–756, Science Press, Beijing, China, 2007, in Chinese, Second edition.

[2] R. S. Aboutaha and R. I. Machado, "Seismic resistance of steel-tubed high-strength reinforced-concrete columns," *Journal of Structural Engineering-ASCE*, vol. 125, pp. 485–494, 1999.

[3] N. E. Shanmugam and B. Lakshmi, "State of the art report on steel-concrete composite columns," *Journal of Constructional Steel Research*, vol. 57, no. 10, pp. 1041–1080, 2001.

[4] D.-Y. Ma, L.-H. Han, and X.-L. Zhao, "Seismic performance of the concrete-encased CFST column to RC beam joint: Experiment," *Journal of Constructional Steel Research*, vol. 154, pp. 134–148, 2019.

[5] Z. Li and Y. S. Su, "Experimental study on seismic behavior of SRC deep beam-to-CFST column frames," *Journal of Constructional Steel Research*, vol. 155, pp. 157–175, 2019.

[6] G. Du, Z. Li, and G. Song, "A PVDF-based sensor for internal stress monitoring of a concrete-filled steel tubular (CFST) column subject to impact loads," *Sensors*, vol. 18, no. 6, p. 1682, 2018.

[7] B. Xu, G. Song, and Y. Mo, "Embedded piezoelectric lead-zirconate-titanate-based dynamic internal normal stress sensor for concrete under impact," *Journal of Intelligent Material Systems and Structures*, vol. 28, no. 19, pp. 2659–2674, 2017.

[8] Y.-F. Yang and F. Fu, "Fire resistance of steel beam to square CFST column composite joints using RC slabs: experiments and numerical studies," *Fire Safety Journal*, vol. 104, pp. 90–108, 2019.

[9] J. Sun and J. Xie, "Simulation analysis of the hydration heat of large diameter CFST arch and its effects on loading age," *Applied Thermal Engineering*, vol. 150, pp. 482–491, 2019.

[10] J. Peng, L. Xiao, J. Zhang, C. S. Cai, and L. Wang, "Flexural behavior of corroded HPS beams," *Engineering Structures*, vol. 195, pp. 274–287, 2019.

[11] L. Huo, C. Li, T. Jiang, and H.-N. Li, "Feasibility study of steel bar corrosion monitoring using a piezoceramic transducer enabled time reversal method," *Applied Sciences*, vol. 8, no. 11, p. 2304, 2018.

[12] J. Peng, S. Hu, J. Zhang, C. S. Cai, and L.-y. Li, "Influence of cracks on chloride diffusivity in concrete: a five-phase mesoscale model approach," *Construction and Building Materials*, vol. 197, pp. 587–596, 2019.

[13] Y. C. Wang, *Steel and Composite-Structures: Behaviour and Design for Fire Safety*, Spon Press, London, UK, 2002.

[14] L.-H. Han and J.-S. Huo, "Concrete-filled hollow structural steel columns after exposure to ISO-834 fire standard,"

Journal of Structural Engineering, vol. 129, no. 1, pp. 68–78, 2003.

[15] J.-B. Yan, X. Dong, and J.-S. Zhu, "Compressive behaviours of CFST stub columns at low temperatures relevant to the Arctic environment," *Construction and Building Materials*, vol. 223, pp. 503–519, 2019.

[16] G. Shan, P. Zhen, X. D. Li, and D. Chen, "Tests on axial strength of circle CFST stub columns under marine atmosphere in cold region," *Construction and Building Materials*, vol. 230, Article ID 117073, 2020.

[17] Y. Yang, Z. C. Gong, H. Deng, L. Zhang, B. Wu, and D. P. Zhao, "Experimental study on fire resistance of cross-shaped concrete filled steel tubular column," *Journal of Building Structures*, vol. 21, pp. 88–96, 2017.

[18] M. Mahsa, H. Amin, X. L. Zhao, and A. P. Jeffrey, "Effect of elevated temperature on the mechanical properties of high-strain-rate-induced partially damaged concrete and CFSTs," *International Journal of Impact Engineering*, vol. 110, pp. 346–358, 2017.

[19] F. Q. Liu, Y. Y. Wang, and L. Gardner, "Experimental and numerical studies of reinforced concrete columns confined by circular steel tubes exposed to fire," *Journal of Structural Engineering*, vol. 145, 2019.

[20] T. Y. Song, Z. Tao, and L. H. Han, "Bond behavior of concrete-filled steel tubes at elevated temperatures," *Journal of Structural Engineering*, vol. 143, 2017.

[21] J. H. Wang, J. He, and Y. Xiao, "Fire behavior and performance of concrete-filled steel tubular columns: review and discussion," *Journal of Constructional Steel Research*, vol. 157, pp. 19–31, 2019.

[22] K. U. Ukanwa, U. Sharma, S. J. Hicks, A. Abu, J. B. P. Lim, and G. C. Clifton, "Behaviour of continuous concrete filled steel tubular columns loaded concentrically in fire," *Journal of Constructional Steel Research*, vol. 136, pp. 101–109, 2017.

[23] K. He, Y. Chen, and S. Han, "Experimental investigation of square stainless steel tubular stub columns after elevated temperatures," *Journal of Constructional Steel Research*, vol. 159, pp. 397–414, 2019.

[24] M. K. Ghanim, Q. L. Qing, and N. S. H. Muhammad, "Numerical analysis of axially loaded rectangular concrete-filled steel tubular short columns at elevated temperatures," *Engineering Structures*, vol. 180, pp. 89–102, 2019.

[25] E. Ellobody, "A consistent nonlinear approach for analysing steel, cold-formed steel, stainless steel and composite columns at ambient and fire conditions," *Thin-Walled Structures*, vol. 68, pp. 1–17, 2013.

[26] K. Zhou and L.-H. Han, "Modelling the behaviour of concrete-encased concrete-filled steel tube (CFST) columns subjected to full-range fire," *Engineering Structures*, vol. 183, pp. 265–280, 2019.

[27] H. Yang and L. H. Han, "Practical calculation method of residual bearing capacity of round steel tube concrete columns after whole process fire," *Engineering Construction & Design*, no. 2, pp. 26–29, 2005.

[28] Q.-H. Tan, L. Gardner, L.-H. Han, and T.-Y. Song, "Fire performance of steel reinforced concrete-filled stainless steel tubular (CFSST) columns with square cross-sections," *Thin-Walled Structures*, vol. 143, p. 106197, 2019.

[29] T.-Y. Song and L.-H. Han, "Post-fire behaviour of concrete-filled steel tubular column to axially and rotationally restrained steel beam joint," *Fire Safety Journal*, vol. 69, pp. 147–163, 2014.

[30] Z. Tao, M. Ghannam, T.-Y. Song, and L.-H. Han, "Experimental and numerical investigation of concrete-filled stainless steel columns exposed to fire," *Journal of Constructional Steel Research*, vol. 118, pp. 120–134, 2016.

[31] F. C. Wang and L. H. Han, "Analytical behavior of special-shaped CFST stub columns under axial compression," *Thin-Walled Structures*, vol. 129, pp. 404–417, 2018.

[32] A. Silva, Y. Jiang, J. M. Castro, N. Silvestre, and R. Monteiro, "Experimental assessment of the flexural behaviour of circular rubberized concrete-filled steel tubes," *Journal of Constructional Steel Research*, vol. 122, pp. 557–570, 2016.

[33] J. Zhang, Y. Li, G. Du, and G. Song, "Damage detection of L-shaped concrete filled steel tube (L-CFST) columns under cyclic loading using embedded piezoceramic transducers," *Sensors (Basel, Switzerland)*, vol. 18, no. 7, 2018.

[34] Q.-X. Ren, L.-H. Han, D. Lam, and C. Hou, "Experiments on special-shaped CFST stub columns under axial compression," *Journal of Constructional Steel Research*, vol. 98, pp. 123–133, 2014.

[35] X. Liu, C. Xu, J. Liu, and Y. Yang, "Research on special-shaped concrete-filled steel tubular columns under axial compression," *Journal of Constructional Steel Research*, vol. 147, pp. 203–223, 2018.

[36] G. Yang, W. L. Cao, H. Y. Dong, W. B. Yang, and S. C. Tian, "Experimental study on eccentric compressive behavior of special-shaped multi-cavity mega-bifurcated concrete filled steel tubular columns," *Journal of Building Structures*, vol. 10, pp. 41–52, 2018.

[37] Y. Y. Wang, Y. L. Yang, S. M. Zhang, and J. P. Liu, "Experimental research on seismic behavior of T-shaped concrete-filled steel tube columns," *Journal of Building Structures*, vol. 400-402, pp. 355–359, 2010.

[38] G. F. Du, C. Ma, and C. X. Xu, "Experimental research on seismic behavior of exterior frame joints with T-shaped CFST column and steel beam," *Advanced Materials Research*, vol. 368-373, pp. 183–188, 2012.

[39] J. C. Zhang and J. Yang, "Study on mechanism of L-shaped concrete-filled steel tubular columns subjected to axial compression," *Advanced Materials Research*, vol. 476-478, pp. 2463–2468, 2012.

[40] JGJ55-2011, *Specification for Mix Proportion Design of Ordinary Concrete*, China Academy of Building Sciences, Beijing, China, 2011, in Chinese.

[41] GB/T50081-2002, *Specification for Test Method of Concrete Mechanical Properties*, China Academy of Building Sciences, Beijing, China, 2007, in Chinese.

[42] GB/T 228.1—2010, *Inspection and quarantine of the people's Republic of China. Metallic Materials—Tensile Testing—Part: 1 Method of Test at Room Temperature*, Standards Press of China, Beijing, China, 2010, in Chinese.

[43] L. H. Xu, G. F. Du, and H. R. Xu, "Experimental study on compression capacity of concrete-filled steel tubular columns with combined T-section," *China Civil Engineering Journal*, vol. 42, no. 06, pp. 14–21, 2009.

[44] S. T. Zhong, *Concrete Filled Steel Tubular Structure*, pp. 1–141, Tsinghua University Press, Beijing, China, 2003, in Chinese.

[45] GB 50010-2010, *Specification for Concrete Structure Design*, China Building Industry Press, Beijing, China, 2010, in Chinese.

[46] J. Lee and G. L. Fenves, "Plastic-damage model for cyclic loading of concrete structures," *Journal of Engineering Mechanics*, vol. 124, no. 8, pp. 892–900, 1998.

[47] F. Wang and G. Song, "Bolt early looseness monitoring using modified vibro-acoustic modulation by time-reversal," *Mechanical Systems and Signal Processing*, vol. 130, pp. 349–360, 2019.

[48] F. Wang, S. C. M. Ho, L. Huo, and G. Song, "A novel fractal contact-electromechanical impedance model for quantitative monitoring of bolted joint looseness," *Institute of Electrical and Electronics Engineers Access*, vol. 6, pp. 40212–40220, 2018.

[49] F. Wang, S. C. M. Ho, and G. Song, "Modeling and analysis of an impact-acoustic method for bolt looseness identification," *Mechanical Systems and Signal Processing*, vol. 133, Article ID 106249, 2019.